geosciences

MDPI

Article

Estimation of Equivalent Pore Aspect Ratio in Rock Physics Models and Validation Using Digital Rocks

Luiz Eduardo Queiroz [1,2,*], Dario Grana [3], Celso Peres Fernandes [2], Tapan Mukerji [4], Leandro Passos de Figueiredo [5] and Iara Frangiotti Mantovani [2]

[1] Petrobras, Rio de Janeiro 20231-030, RJ, Brazil
[2] Department of Mechanical Engineering, Federal University of Santa Catarina, Florianópolis 88035-972, SC, Brazil; celso@lmpt.ufsc.br (C.P.F.); iara@lmpt.ufsc.br (I.F.M.)
[3] Department of Geology and Geophysics, University of Wyoming, Laramie, WY 82071-2000, USA; dgrana@uwyo.edu
[4] Stanford University, Stanford, CA 94305, USA; mukerji@stanford.edu
[5] LTrace, Florianópolis 88034-480, SC, Brazil; leandro@ltrace.com.br
* Correspondence: eduardoqueiroz@petrobras.com.br

Abstract: Complex pore structures with multiple inclusions challenge the predictive accuracy of rock physics models. This study introduces a novel method for estimating a single equivalent pore aspect ratio that optimizes rock physics model predictions by minimizing discrepancies with experimental measurements in porous rocks with multiple inclusions with variable aspect ratios and proportions. The proposed methodology uses digital rock physics numerical simulations for validation. A comparative analysis is conducted between the equivalent aspect ratio derived from optimized rock physics models, numerical simulations, and the aspect ratio distribution estimated from digital rock samples. The approach is tested on both synthetic and real core samples, demonstrating its robustness and applicability to field data, including core samples and well log data. The validation results confirm that the method enhances predictive accuracy and offers a versatile framework for addressing pore complexity in subsurface rock formations.

Keywords: rock physics; digital rock physics; reservoir geophysics; carbonate rocks

check for updates

Academic Editor: Hongyuan Liu

Received: 13 January 2025
Revised: 8 February 2025
Accepted: 10 February 2025
Published: 15 February 2025

Citation: Queiroz, L.E.; Grana, D.; Fernandes, C.P.; Mukerji, T.; de Figueiredo, L.P.; Mantovani, I.F. Estimation of Equivalent Pore Aspect Ratio in Rock Physics Models and Validation Using Digital Rocks. *Geosciences* **2025**, *15*, 67. https://doi.org/10.3390/geosciences15020067

Copyright: © 2025 by the authors. Licensee MDPI, Basel, Switzerland. This article is an open access article distributed under the terms and conditions of the Creative Commons Attribution (CC BY) license (https://creativecommons.org/licenses/by/4.0/).

1. Introduction

Rock physics is a branch of exploration geophysics that investigates relationships between the physical and mechanical properties of rocks and their geophysical responses. Specifically, it involves understanding how factors such as mineral composition, porosity, permeability, fluid saturation, pressure, and temperature influence rock properties like seismic velocity, density, elastic moduli, electrical resistivity, dielectric properties, thermal conductivity, and nuclear magnetic resonance. We focus on the application of rock physics to seismic reservoir characterization studies and the relationships between porosity, mineral composition, and fluid saturation, and their elastic properties, including P- and S-wave velocities and density. These relationships are fundamental for interpreting subsurface properties and can be derived from laboratory measurements of rock samples or well log data. A rock physics model (RPM) represents this relationship through a set of equations that link petrophysical and elastic properties, providing essential tools for subsurface characterization [1].

RPMs generally rely on theoretical predictions of the elastic response of rocks based on the volumetric fractions, properties, and geometric arrangements of their components.

These models enable the estimation of equivalent elastic properties as well as their upper and lower bounds. These models are generally calibrated using core samples and well logs to define the optimal values of empirical parameters that cannot be measured at the field scale. However, because of the natural heterogeneity and variability of porous rocks, the values of the RPM parameters are not unique and may vary in space, from one interval to another, and even within the same core samples. Hence, the calibration of RPMs often aims to find some effective parameters that average the values of the underlying distributions. This average is not always linear, and the calculation of effective rock properties is still an ongoing research topic [1].

This work focuses on carbonate rocks, known for their genetic and diagenetic complexity, where the pore structure dominates the elastic response and the elastic properties are largely influenced by the pore geometry [2,3]. For this reason, inclusion-based RPMs are suitable for modeling rock physics relations in carbonate rocks [1]. Inclusion models aim to represent a porous rock as a solid material with multiple inclusions with different shapes and sizes. Pore geometry is mathematically represented by a set of parameters describing the proportions, shapes, sizes, and orientations of the pores. Several models are based on the assumption that pores can be described by ellipsoids, or oblate and prolate spheroids, whose size can be described by a parameter commonly referred to as aspect ratio, which effectively captures the spatial complexity of pore geometry [1], with several models proposed for predicting elastic moduli and velocities in media with multiple inclusions [1,4–10].

Rock physics models incorporating inclusions have been developed for understanding the elastic properties of heterogeneous rocks, particularly in carbonate reservoirs. The pioneering work of Budiansky [4] laid the foundation for effective medium theories, providing an initial framework for modeling the elastic behavior of composite materials. Mori and Tanaka [5] introduced the Mori–Tanaka scheme, which estimates the average stress and strain fields in a matrix with inclusions, a method later extended by Kuster and Toksöz [6] to model seismic wave velocities and attenuation in two-phase media. Further refinements were achieved by Norris [9], who developed a differential effective medium scheme to better capture the moduli variations in composite materials. Berryman [7] applied long-wavelength approximations to analyze wave propagation in media containing spherical inclusions, a key contribution that was later expanded to account for fluid-saturated porous rocks [8]. Applications of these theoretical models to carbonate rocks have demonstrated their effectiveness in characterizing complex pore structures. Xu and Payne [11] employed inclusion-based models to predict the elastic properties of carbonate reservoirs, highlighting the influence of pore shape and connectivity. Sun [12] explored how pore structures affect elastic wave propagation, emphasizing the importance of accurate AVO modeling in porous media. Further, Dou et al. [13] demonstrated that rock physics models could be used to evaluate permeability heterogeneity in carbonate reservoirs by integrating pore type characterization with geophysical measurements. Experimental studies by Li et al. [14] provided additional insights into the effects of fractures on acoustic wave propagation using synthetic borehole models. Numerical simulations have also contributed significantly to understanding composite inclusions; for instance, Garboczi and Berryman [10] compared effective medium theories with finite element computations, offering a robust validation of the theoretical predictions. These studies collectively highlight the importance of inclusion-based models in rock physics, demonstrating their applicability in seismic interpretation, reservoir characterization, and borehole acoustic analysis. As modeling techniques continue to evolve, integrating experimental data with advanced numerical methods will further enhance the predictive capabilities of rock physics frameworks.

These models are often used in fractured rocks, where the fractures are described as elliptical shapes characterized by their aspect ratio and proportion. In fractured rocks, non-interaction approximation theory [15] reliably estimates the effective elasticity, even with closely spaced or intersecting fractures, offering accurate predictions for crack densities with minor stiffening effects from stress field interactions. The resulting crack-induced anisotropy remains approximately orthorhombic, making this approach practical for seismic and reservoir characterization.

However, in carbonate reservoirs with high heterogeneity, the variability of the pore geometry makes RPMs based on a single inclusion inadequate. Several publications have investigated the effect of aspect ratio on elastic properties [11,16–18]. Xu and Payne [11] categorized pores into stiff, interparticle, and crack types based on aspect ratios. Dias et al. [18] adopted dual-porosity approaches to distinguish stiff and compliant pores. Fournier et al. [16] highlighted the value of using the aspect ratio in quantifying diagenetic effects and defining pore types. Wang et al. [17] demonstrated that aspect ratio influences velocities more than pore size. However, aspect ratio cannot be measured directly in many practical applications. Some empirical relations have been derived using laboratory measurements to relate aspect ratio to porosity and mineral volumes in specific core samples [19,20], but the generalization of these relations is very challenging.

Recent advances in digital rock physics (DRP) have improved our understanding of the complex structure of carbonate rocks and the validation of rock physics models at the pore scale [21–23]. For example, Weger et al. [24,25] employed digital image analysis to assess pore size and network complexity. Furthermore, DRP leverages numerical simulations to study the elastic response of porous rocks, enabling detailed analysis of their mechanical properties. Finite-difference simulations applied to a fine-scale grid, defined on the rock's digitized microstructure, are used to solve linear elasticity equations with boundary constraints mimicking stress or strain conditions, which enables the computation of bulk and shear moduli [26]. The gained knowledge about pore geometry in carbonate rocks has led to advancements in seismic reservoir characterization of carbonate reservoirs thanks to the integration of RPMs with seismic methods for the estimation of pore structure characteristics, such as aspect ratio and orientation, from well logs and seismic data [27–31].

To improve RPM predictions in complex pore structures, this study aims to define a method for estimating an equivalent pore aspect ratio (EPAR). We define the EPAR as the aspect ratio value that minimizes the mismatch between measurements and model predictions. Validation is achieved using DRP numerical simulations based on 3D digital representations of rocks obtained by X-ray micro-computed tomography (micro-CT) [21,22]. The proposed approach is tested on synthetic and real digital samples, demonstrating its potential for application to core measurements and well log data. By comparing the equivalent pore aspect ratio estimated from the optimized RPM with numerical simulations and the distribution of aspect ratios from digital rocks, this work provides a robust framework for addressing the inherent complexity of carbonate rock pore structures.

We validate the EPAR definition by analyzing idealized rock geometries with varying porous inclusions, comparing RPM predictions and DRP numerical simulations using digital samples of synthetic and real rocks and estimating the EPAR by fitting an RPM to DRP simulations. The results are also discussed and validated in the context of well log data analysis for a dataset in a Brazilian pre-salt reservoir.

2. Methods

2.1. Rock Physics Models

A porous rock is generally modeled as a composite medium consisting of three components: the matrix (a mixture of N_m minerals with known proportions), the porous structure,

and the fluid (or fluid mixture) filling the pores. In this work, we assume that the matrix properties are known, including the bulk modulus K_m and shear modulus μ_m [1]. The focus of this work is on the effective elastic properties of the pore skeleton, including the matrix and the pore space. Inclusion models assume that the pore structure is modeled as N_p phases of inclusions, which may represent solid phases or pores. These models derive equations based on stress equilibrium in the effective medium due to phase interactions [1]. We apply four inclusion-based formulations to characterize the stiffness of the pore skeleton.

The Mori–Tanaka (MT) formulation [1,5] assumes that the effect of each inclusion on the effective stress is equivalent to its behavior as a single inclusion. This approach provides explicit expressions for the effective elastic moduli, K_{MT}^{eff} and μ_{MT}^{eff}:

$$\sum_{i=1}^{N_p} x_i(K_i - K_{MT}^{eff})P_i^0 = 0 \tag{1}$$

$$\sum_{i=1}^{N_p} x_i(\mu_i - \mu_{MT}^{eff})Q_i^0 = 0, \tag{2}$$

where N_p is the number of components, index i refers to the i-th material with bulk and shear moduli K_i and μ_i, index 0 refers to the matrix, x represents the volume fraction, and P_i^0 and Q_i^0 are the geometric factors of the inclusions. The expressions for the factors P_i^m and Q_i^m are defined in the literature for multiple shapes of inclusions, such as spheres, needles, disks, penny cracks, and ellipsoidal [1]. For elliptical inclusions, these factors depend only on the aspect ratio α, defined as the ratio between the minor and major semi-axes of the ellipsoid in 3D or ellipse in 2D. The analytical expressions are described in Appendix A.

The Kuster–Toksöz (KT) formulation [6] for seismic velocities is based on first-order scattering theory. This formulation was generalized in [7] for the calculation of the effective elastic moduli, K_{KT}^{eff} and μ_{KT}^{eff}, as

$$(K_{KT}^{eff} - K_0)\frac{(K_0 + 4/3\mu_0)}{(K_{KT}^{eff} + 4/3\mu_0)} = \sum_{i=1}^{N_p} x_i(K_i - K_0)P_i^0 = 0 \tag{3}$$

$$(\mu_{KT}^{eff} - \mu_0)\frac{(\mu_0 + \zeta_0)}{(\mu_{KT}^{eff} + \zeta_0)} = \sum_{i=1}^{N_p} x_i(\mu_i - \mu_0)Q_i^0 = 0, \tag{4}$$

where

$$\zeta = \frac{\mu(9K + 8\mu)}{6(K + 2\mu)}. \tag{5}$$

The self-consistent (SC) approximation [4] is based on the deformation of isolated inclusions, and the interactions between inclusions are approximated by assuming the matrix with known effective moduli. This formulation was generalized in [32] for a mixture of N_p components, where the effective elastic moduli K_{SC}^{eff} and μ_{SC}^{eff} are calculated as

$$\sum_{i=0}^{N_p} x_i(K_i - K_{SC}^{eff})P_i^{eff} = 0 \tag{6}$$

$$\sum_{i=0}^{N_p} x_i(\mu_i - \mu_{SC}^{eff})Q_i^{eff} = 0, \tag{7}$$

where the matrix is considered one of the components of the mixture and the geometric factors are defined using inclusions in the effective medium rather than inclusions in the matrix (P_i^{eff}, Q_i^{eff} instead P_i^0, P_i^0).

Finally, the differential effective medium (DEM) model [9] assumes incremental inclusions of an additional phase into a matrix. Additional inclusions are added until the desired proportion is reached. For multiple inclusion shapes, each constituent is added independently. The model predictions depend on the order of inclusions. The mathematical formulation consists of a system of coupled nonlinear ordinary differential equations [1,32], where the effective elastic moduli K_{DEM}^{eff} and μ_{DEM}^{eff} are calculated as

$$(1-y)\frac{d}{dy}[K_{DEM}^{eff}(y)] = (K_2 - K_{DEM}^{eff})P^{eff\,2}(y) \quad (8)$$

$$(1-y)\frac{d}{dy}[\mu_{DEM}^{eff}(y)] = (\mu_2 - \mu_{DEM}^{eff})Q^{eff\,2}(y), \quad (9)$$

with initial conditions $K_{DEM}^{eff}(0) = K_1$ and $\mu_{DEM}^{eff}(0) = \mu_1$, where K_1 and μ_1 are the elastic moduli of the background matrix, K_2 and μ_2 are the elastic moduli of the inclusion, P_i^m and Q_i^m are the geometric factors of the inclusion, and y is the concentration of the inclusion.

All these models can be used to compute the effective properties of dry rocks (i.e., the pore skeleton with empty pores) or saturated rocks (i.e., the pore skeleton with fluid-filled pores). In general, the fluid phase is a mixture of several components, such as oil, water, and gas, and the effective bulk modulus of the mixture depends on the properties of each component and their proportions. There are two strategies for modeling saturated-rock elastic properties, either considering the fluid as an inclusion or modeling empty inclusions and computing the saturated properties using Gassmann's equations [1]. In this work, we focus on the dry rock properties since core sample measurements and digital rock physics simulations are conducted on dry rocks.

2.2. Digital Rock Physics

DRP enhances the understanding of complex pore structures in porous rocks by imaging the geometry of the pore network and computing elastic properties using finite-difference simulations [21–26]. The DRP workflow for computing elastic properties includes three steps: (a) imaging to obtain a high-resolution 3D image; (b) processing to segment the matrix and pore phases; and (c) simulating the physical process on the numerical grid to compute effective properties [21,22,26]. This technique has been applied to image carbonate rocks and to improve the understanding of their complex structure [23]. In this work, digital rock physics (DRP) is used for validation purposes.

In this work, DRP methods are used to compute elastic properties of core samples using their digital images. Several approaches have been presented to estimate the elastic moduli of digital samples, including static methods that impose equilibrium boundary conditions and dynamic methods that simulate wave propagation. These methods are based on the numerical solution of differential equations using finite differences or finite element algorithms [26,33]. We use the software GeoDict [34] to calculate the effective elastic properties of the digital rocks. GeoDict provides two algorithms, namely FeelMath and LIR, to compute the elastic properties of complex micro-structures by solving a system of partial differential equations on the 3D image and computing the local stresses and strains, the stiffness tensor, and anisotropic properties [34,35].

From the image segmented into phases, it is possible to measure parameters describing the pore network's morphology and spatial organization, such as porosity, pore size distribution, tortuosity, and spatial correlation functions. Specifically, we can estimate the distribution of aspect ratio in the sample using digital images. The image analysis process was accomplished using Avizo3D software [36]. Before segmenting the digital image into matrix and pore phases, we applied a combination of two filters: non-local means [37] and unsharp masking [38]. The filters smooth the original image, reducing noise and enhancing

the phase contrast. Subsequently, we used the watershed algorithm [39] to separate the pore phase into individualized objects and measure their volume, surface area, Feret diameter, elongation, and aspect ratio [24,25,40].

2.3. Estimation of Equivalent Pore Aspect Ratio

Many inclusion-based RPMs use the aspect ratio to parameterize the pore shape and size. However, aspect ratio cannot be measured in many practical applications. Furthermore, direct measurements of the proportions of the different inclusion types are generally not available. Hence, we propose to estimate the aspect ratio as a solution of an inverse problem, where we optimize an inclusion-based RPM with a single (effective) inclusion using measurements of elastic properties, either bulk and shear moduli or P- and S-wave velocities. In this context, and consistently with previous definitions in the literature [16,30,41], we define the EPAR as the value of the aspect ratio that minimizes the mismatch between rock physics model predictions and measurements for a given parameterization of elastic properties. The result is an effective value $\hat{\alpha}$ that represents an average, not necessarily linear, of the aspect ratios $\alpha_1, \alpha_2, ...\alpha_N$ of N inclusions. For this reason, we consider it an EPAR.

As commonly suggested for the calibration of the rock physics model using ultrasonic measurements, we recommend computing the estimation of the EPAR using dry rock measurements to avoid fluid effect interference caused by dispersion in laboratory experiments. In this case, we adopt a parameterization in terms of elastic moduli. Hence, the EPAR $\hat{\alpha}$ is computed as the optimal parameter that minimizes the mismatch between predictions and measurements:

$$\hat{\alpha} = \underset{\alpha}{\operatorname{argmin}} \left[\sigma_K \left(K^{RPM}(\alpha) - K^{data} \right)^2 + \sigma_\mu \left(\mu^{RPM}(\alpha) - \mu^{data} \right)^2 \right], \tag{10}$$

where $K^{RPM}(\alpha)$ and $\mu^{RPM}(\alpha)$ are the bulk and shear moduli predicted by the RPM; K^{data} and μ^{data} are the measured elastic moduli (from core analysis, well logs, or DRP images); and σ_K and σ_μ are weighting factors. We use $\sigma_K = 1/K_m^2$ and $\sigma_\mu = 1/\mu_m^2$, to normalize the residuals of the elastic moduli on the same scale. Based on this definition, the EPAR represents the value of the aspect ratio of an effective pore network that has the same elastic response as the real pore network.

The calculation in Equation (10) can be applied to different input data, for example, laboratory measurements of elastic moduli or sonic logs. In the case of laboratory experiments, analysis is generally conducted on dry samples to avoid the fluid effect; hence, the proposed optimization can be applied directly to the measurements. Instead, in the case of sonic logs, saturated-rock elastic moduli are first computed from P- and S-wave velocities, and the dry-rock elastic moduli are estimated using Gassmann's equation. Alternatively, Equation (10) can be formulated in terms of velocities and applied directly to well logs.

One of the novelties of the approach in this work is the validation using DRP. In this work, we estimate the distribution of the aspect ratio from digital rocks. For each pore of the digital image, we estimate the aspect ratio of the pore. This implies that we can apply the RPM using the full distribution of aspect ratios. In other words, we can apply any RPM formulation in the Section Rock Physics model with as many inclusions, with their corresponding aspect ratio, as detected from the digital images. For MT, KT, and SC, the calculation is straightforward using Equations (1)–(7), whereas, for the DEM, the calculation is challenging when the number of inclusions is relatively large. Hence, using the RPMs with the full distribution of aspect ratios (and setting the data equal to the RPM predictions), we can compute an EPAR value. However, as discussed in Section "Digital rock physics", numerical simulations can be performed to compute the effective elastic

properties. Hence, using the DRP numerical simulations (and setting the data equal to the DRP simulated values), we can also compute an EPAR value and compare the values computed by optimizing RPM and DRP estimations.

3. Results

This section validates the definition of the Effective Pore Aspect Ratio (EPAR) by analyzing idealized rock geometries with different types of porous inclusions across varying volumetric proportions. Then, the analysis compares RPM predictions with DRP using synthetic digital samples with idealized geometry. Next, the EPAR is estimated by fitting an RPM with a single effective inclusion to DRP simulations of sub-samples from real digital rock images. The study then extends to digital images of real rocks, utilizing public data from outcrop samples. The EPAR is computed using the full distribution of aspect ratios computed using GeoDict. Finally, the validity of the investigation is demonstrated through well log data from a carbonate reservoir in Brazil's pre-salt region, with analyses of two core samples extracted from the reservoir.

3.1. Evaluation of EPAR from Multiple Inclusions Using RPM

We first validate the definition of EPAR assuming geometrically idealized rocks with two types of porous inclusions, with aspect ratios α_1 and α_2, for different volumetric proportions.

We first calculate the values of the elastic moduli using the RPM. Then, we fit the EPAR values using Equation (10). Based on the rock physics formulations, the EPAR is a function of the porosity (ϕ), bulk and shear moduli of the matrix (K_m and μ_m), aspect ratios of the inclusions (α_1 and α_2), and volumetric proportions of the inclusions (p and $1-p$). Figure 1 shows the sensitivity of EPAR to these parameters for the DEM model. The results show higher sensitivity to variations in aspect ratio, limited sensitivity to porosity and matrix elastic moduli, and increased sensitivity to low aspect ratios. We test four different models using Equations (3)–(9). For simplicity, we only show the full results for the DEM model, but the MT, KT, and SC models demonstrate similar behavior. Figure 2 shows the results for variable porosity and aspect ratios of two inclusions and proves that, for each rock physics model, it is possible to compute the EPAR for all combinations of aspect ratios and proportions for all pore volume values. These results show that the EPAR is not a linear average of the aspect ratios weighted by their proportions but rather follows a nonlinear average.

Table 1 shows the average errors between the bulk and shear moduli predicted by the rock physics models for two inclusion types and those calculated using a single EPAR. The parameters are the same as in Figure 1. For the DEM, we test the model by adding the two inclusions in two different orders. Overall, a single EPAR value enables us to fit the elastic moduli computed using the RPM with high accuracy and low errors.

Table 1. Average relative errors between bulk and shear moduli calculated by RPM with two inclusion types and RPM with single equivalent inclusion. The RPM parameters are the reference values in Figure 1.

Elastic Moduli Error	MT	KT	SC	DEM (α_1, α_2)	DEM (α_2, α_1)
Bulk modulus	−0.164%	−0.126%	−0.150%	−0.191%	−0.057%
Shear modulus	0.007%	0.019%	0.003%	0.295%	0.081%

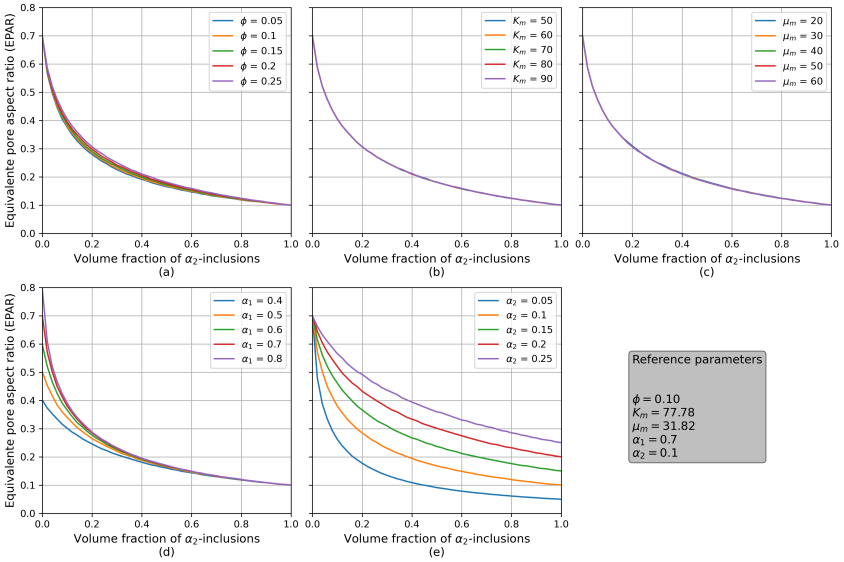


Figure 1. Sensitivity of equivalent pore aspect ratio (EPAR) to RPM parameters. The EPAR values are obtained by optimizing the aspect ratio value of a single inclusion. The EPAR values are plotted as function of the volume fraction of the inclusions with aspect ratio α_2. Their variations are shown with respect to multiple values of the following parameters: porosity ϕ (**a**), matrix bulk modulus K_m (**b**), matrix shear modulus μ_m (**c**), aspect ratio of inclusion 1 α_1 (**d**), and aspect ratio of inclusion 2 α_2 (**e**). In each plot, one parameter varies, whereas the others are kept constant and equal to the reference parameters.

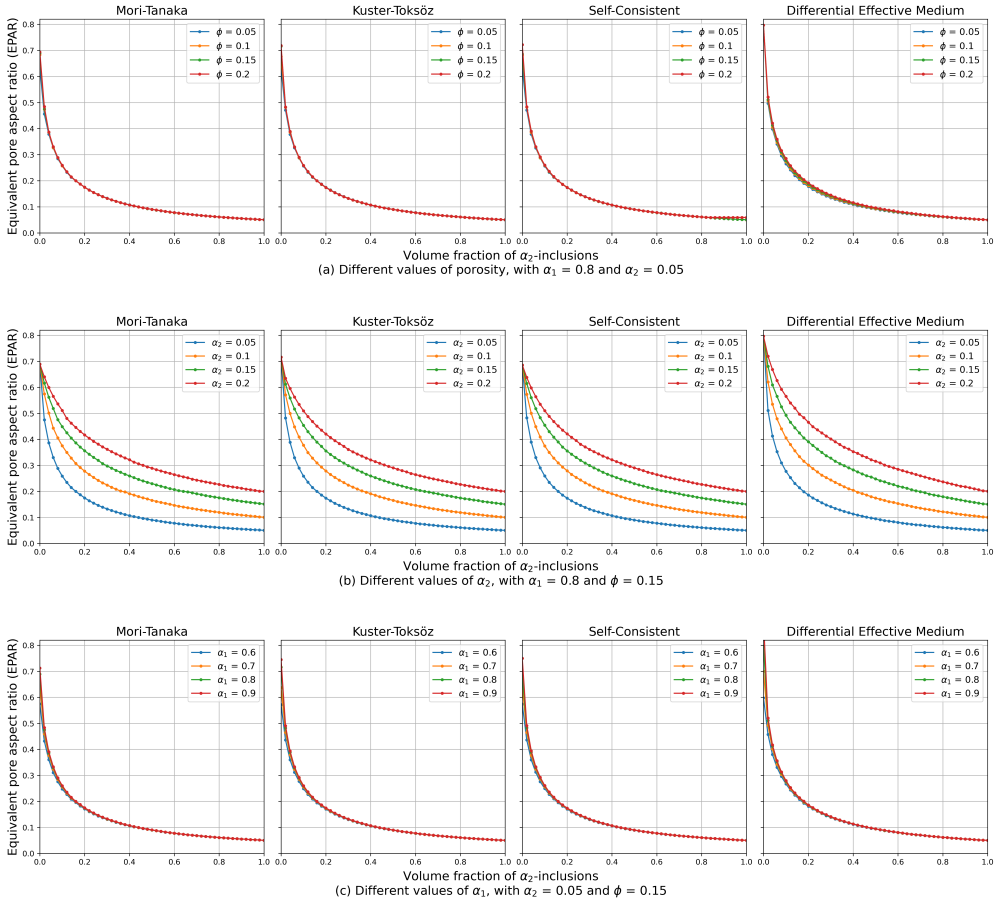


Figure 2. Equivalent pore aspect ratio (EPAR) for porous medium with inclusions of aspect ratios α_1 and α_2 and variable volumetric proportions for different rock physics models. The colored lines represent predictions for different values of (**a**) porosity, (**b**) α_2, and (**c**) α_1. In each plot, one parameter varies, whereas the others are kept constant and equal to the reference parameters.

We then extend this approach to porous rocks with three types of inclusions with aspect ratios α_1, α_2, and α_3. To illustrate the applicability to three inclusions, we choose values $\alpha_1 = 0.1$, $\alpha_2 = 0.2$, and $\alpha_3 = 0.8$ and assume $\phi = 0.05$, $K_m = 77.78$, and $\mu_m = 31.82$. We calculate the bulk and shear moduli using the RPMs and then find the EPAR to match the RPM predictions with three inclusions and the RPM predictions with a single equivalent inclusion. The value depends on the volumetric fractions of the inclusions. Figure 3a shows the EPAR for different volumetric fractions of α_1-inclusions, α_2-inclusions, and α_3-inclusions (obtained as one minus the sum of the other two volumetric fractions). For example, the black star indicates that, for a rock with volumetric fractions of inclusions of 0.2, 0.2, and 0.6 with aspect ratios $\alpha_1 = 0.1$, $\alpha_2 = 0.2$, and $\alpha_3 = 0.8$, respectively, the corresponding EPAR is 0.24. The limiting cases, where one of the volumetric fractions is zero, are shown in Figure 3b. For simplicity, only the results for DEM are shown, but the results are similar for the other RPMs. Table 2 shows the average relative errors between the bulk and shear moduli calculated using the three aspect ratios and those calculated using EPARs for different rock physics models. Overall, all the models produce accurate results using only a single EPAR value.

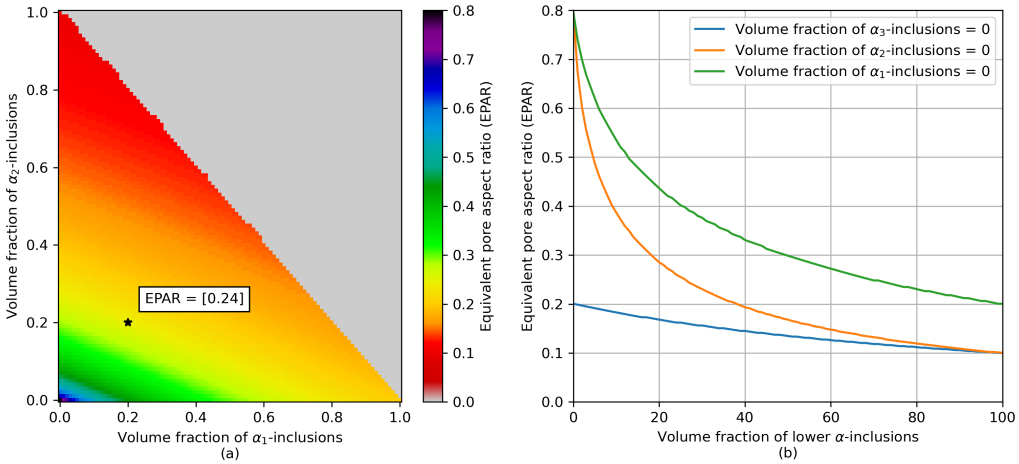


Figure 3. EPAR for porous rocks with 3 inclusion types: (**a**) EPAR variations for variable inclusion proportions and (**b**) EPAR variations in limiting cases with two inclusions only.

Table 2. Average relative errors between bulk and shear moduli calculated by RPM with three inclusion types and RPM with single equivalent inclusion. The RPM parameters are $\alpha_1 = 0.1$, $\alpha_2 = 0.2$, $\alpha_3 = 0.8$, $\phi = 0.05$, $K_m = 77.78$, and $\mu_m = 31.82$.

Elastic Moduli Error	MT	KT	SC	DEM (α_1, α_2,α_3)
Bulk modulus	0.101%	0.102%	0.106%	0.021%
Shear modulus	0.021%	0.015%	0.015%	−0.043%

3.2. Comparison between DRP Simulations and RPM Predictions

In this section, we first compare RPM predictions with DRP numerical simulations using synthetic digital samples with idealized geometry with constant aspect ratios for one and two inclusions. Then, we demonstrate the calculation of the EPAR estimated by fitting an RPM with a single effective inclusion with the EPAR to DRP numerical simulations using sub-samples of real digital images.

3.2.1. Synthetic Digital Samples

We first generate synthetic digital images with idealized geometry. The images are generated by randomly adding ellipsoidal inclusions at random spatial positions until the volume fraction of the inclusions reaches the desired porosity (Figure 4). This approach

enables generating synthetic digital images of porous media with different porosity values. The bulk and shear moduli of the solid matrix are assumed to be known and equal to $K_m = 77.78$ GPa and $\mu = 31.82$ GPa, respectively. Initially, we generate digital images with constant aspect ratios. For this test, we choose six different values of aspect ratio, specifically 0.1, 0.2, 0.3, 0.4, 0.5, and 1.001.

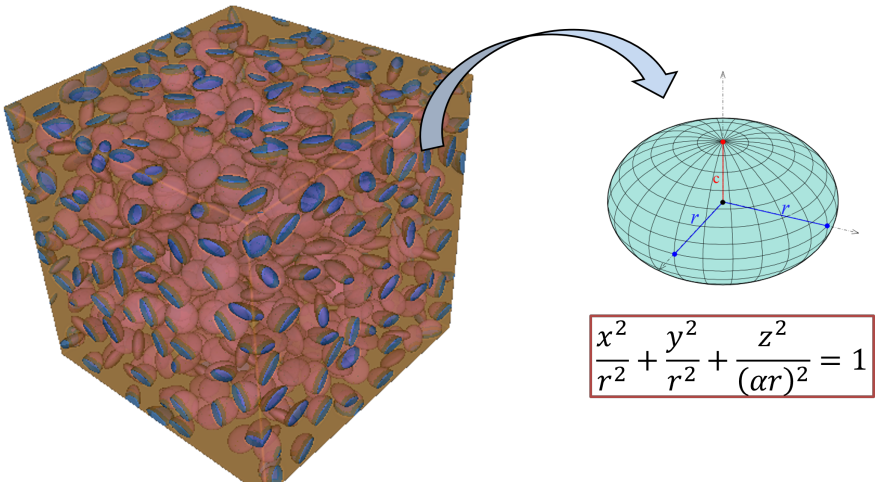


Figure 4. Example of synthetic digital sample with ellipsoidal inclusions.

Figure 5 shows the comparison in terms of bulk and shear moduli between the RPM predictions (for models MT, KT, SC, and DEM) and numerical simulations obtained using GeoDict [34]. The stars represent the numerical results, and the lines represent the RPM predictions for different values of porosity and aspect ratio.

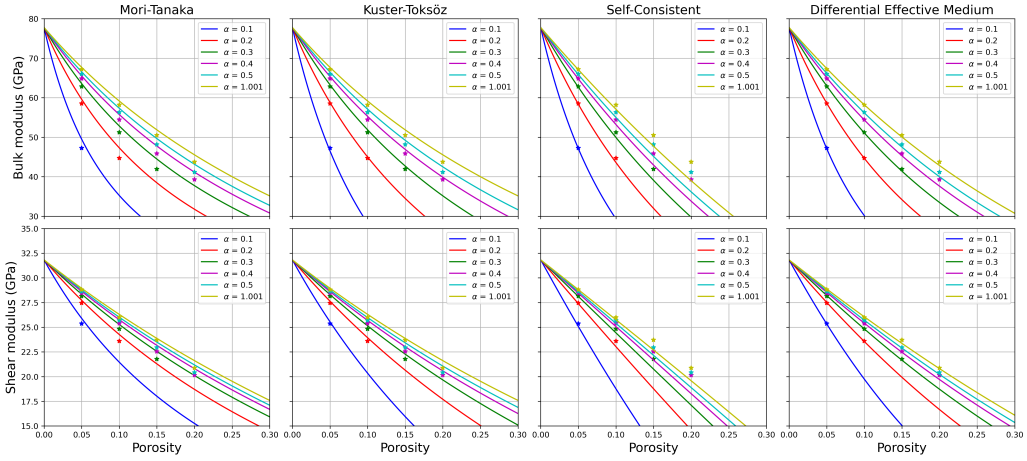


Figure 5. Comparison between RPM predictions and DRP numerical simulations for synthetic digital images with constant aspect ratio for bulk and shear moduli. The stars represent the values of the numerical simulations, and the lines represent the RPM predictions.

Figure 6 shows the relative errors between the elastic moduli predicted by the four RPM models and those calculated using the DRP numerical simulations. The errors increase with increasing porosity for all the models. Furthermore, the MT and KT models always overestimate the values, while the SC model always underestimates the values. The DEM models provide the lowest errors, which is consistent with common knowledge that DEM models are more accurate in media with isolated inclusions [1].

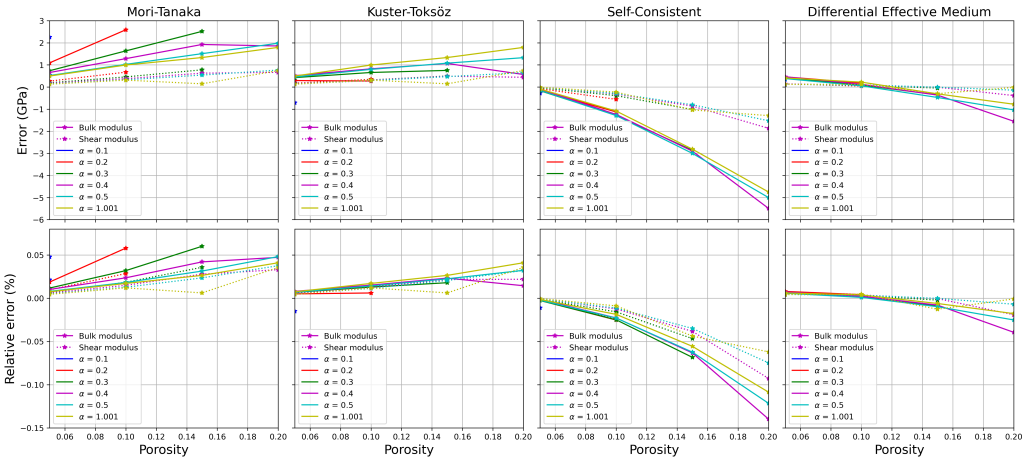


Figure 6. Relative error between RPM predictions and DRP numerical simulations for synthetic digital images for bulk and shear moduli.

We then generate synthetic images with two types of inclusions, with aspect ratios $\alpha_1 = 0.9$ and $\alpha_2 = 0.3$, and variable volumetric proportions. As in the previous example, we calculate the bulk and shear moduli using RPM and DRP simulations. Figure 7 shows the comparison of the values predicted by the RPMs and those obtained using the DRP numerical simulations. Overall, errors increase with increasing porosity, and the DEM predictions are the closest to the DRP numerical simulations.

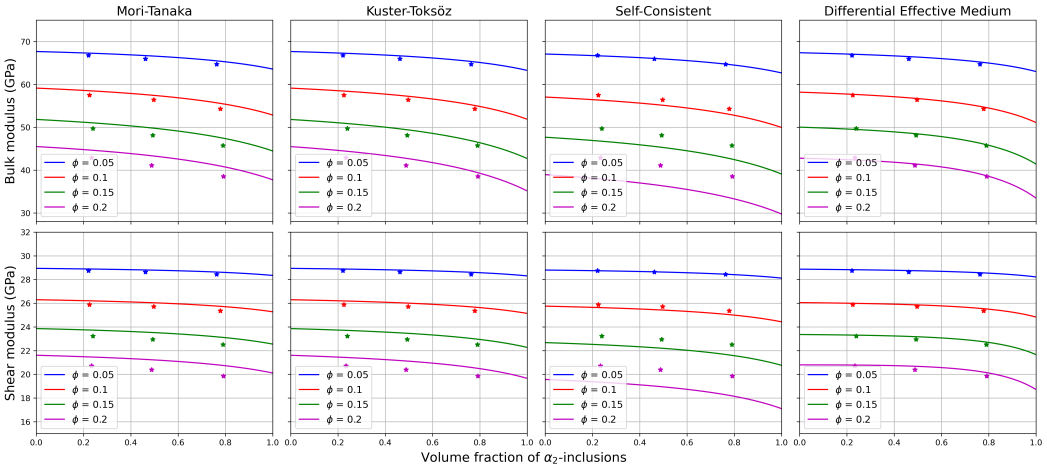


Figure 7. Comparison between RPM predictions and DRP numerical simulations for synthetic digital images with two inclusion types with aspect ratios $\alpha_1 = 0.9$ and $\alpha_2 = 0.3$ for bulk and shear moduli. The stars represent the values of the numerical simulations, and the lines represent the RPM predictions.

3.2.2. Real Digital Samples

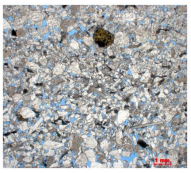
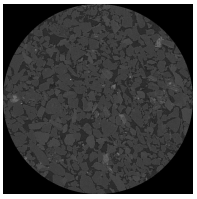
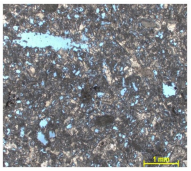
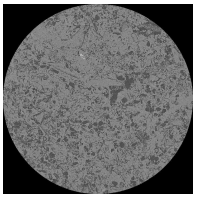
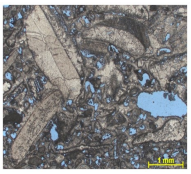
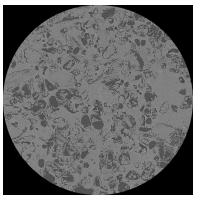
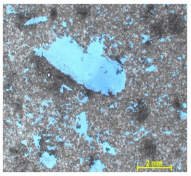
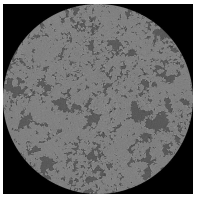
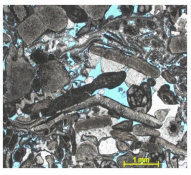
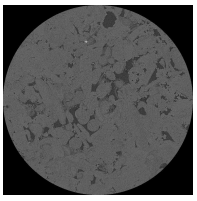
We then extend our analysis to digital images of real rocks. For the following tests, we use public data of samples from outcrops from different regions of the United States. For each outcrop, three plugs were cut and laboratory measurements were taken, and two smaller samples were extracted from one of these plugs and imaged by microtomography, resulting in ten digital rock samples. The outcrop samples and their petrographic descriptions are as follows:

- Desert Pink (DP): Fine, poorly sorted bioclastic grainstone, cemented by calcite, with little compaction. High porosity of the granular, moldic, and intercrystalline types;

- Edwards Yellow (EY): Fine, poorly sorted bioclastic grainstone, cemented by calcite with intense dissolution. High porosity of the intragranular, moldic, intercrystalline, and intergranular types;
- Indian Limestone (IL): Coarse bioclastic grainstone, moderately poorly sorted, intensely cemented by calcite. Very low porosity of the intergranular and intercrystalline types;
- Silurian Dolomite (SD): Medium to coarse dolomite. High porosity of the intercrystalline and vugular types;
- Boise SS (BOS): Medium sandstone, moderately sorted. Good porosity of the intergranular, intragranular, and moldic types.

Table 3 shows thin sections and micro-CT images of the samples.

Table 3. Summary of available rock samples.

Code	Name	Classification	Thin Section	CT Image
BOS	Boise SS	Sandstone		
DP	Desert Pink	Bioclastic Grainstone		
EY	Edwards Yellow	Bioclastic Grainstone		
SD	Silurian Dolomite	Dolomite		
IL	Indiana Limestone	Bioclastic Grainstone		

Using DRP tools, after pre-processing, filtering, and segmentation, we computed the porosity and numerically calculated the elastic moduli using GeoSlicer [42,43] and GeoDict [34] software. The digital samples are stored in grids of 1200 × 1200 × 1200 pixels with a resolution of 3 μm. We then divided each sample into eight sub-samples of equal dimensions and obtained eighty digital samples, including eight sub-samples for each digital image of the two samples of the five rock types (DP, EY, IL, SD, and BOS). Figure 8 shows the porosity and elastic moduli numerically calculated using DRP for each of the eighty sub-samples. The colors represent each type of sample.

We then apply the RPMs to compute the RPM predictions of the elastic moduli. The dashed-dotted lines show the RPM values predicted by the DEM for three different aspect ratios α equal to 0.1, 0.2, and 0.3, plotted for comparison. The RPMs assume constant mineralogical compositions consistent with laboratory analyses: calcite for the DP, EY, and IL samples, dolomite for the SD samples, and quartz for the BOS samples. The elastic moduli are $K_m^{cal} = 77.78$ and $\mu_m^{cal} = 31.82$ for calcite, $K_m^{dol} = 91$ and $\mu_m^{dol} = 41$ for dolomite, and $K_m^{qtz} = 36$ and $\mu_m^{qtz} = 45$ for quartz.

We then estimate the EPAR using the proposed optimization approach, where we aim to match numerically calculated values of bulk and shear moduli. Figure 9 shows the values of EPARs using the MT, KT, SC, and DEM for a single inclusion for all the 80 sub-samples. At low porosity (for example, in the IL samples), the EPAR values of the four different RPMs are similar, whereas, at high porosities, the four different models lead to different EPAR values, especially for the SC model. Figure 10 shows the elastic moduli numerically calculated using DRP (marked with circles) and the elastic moduli calculated using RPMs with the calculated EPARs (marked with crosses). Overall, the RPM predictions and the DRP values match.

Table 4 shows the mean and standard deviation of the relative errors between the values found using the RPM with the respective EPARs in relation to the values obtained numerically from the digital images. In all the models, the adjusted bulk modulus is slightly larger than the measured value, while the shear modulus is slightly smaller. We note that the SC model was better suited for real samples, with errors on the order of 1%, while the KT showed the worst results, with average errors greater than 10%.

Table 4. Mean and standard deviation of the relative errors between the values of the bulk and shear moduli numerically calculated by DRP and values calculated using RPM with EPAR estimated using 80 sub-samples of digital images.

Elastic Moduli Error		**MT**	**KT**	**SC**	**DEM**
Bulk modulus	Mean	−7.133%	−8.703%	−1.265%	−4.707%
	Standard deviation	4.094%	5.622%	0.925%	2.591%
Shear modulus	Mean	6.690%	10.720%	1.138%	4.605%
	Standard deviation	2.883%	5.317%	0.803%	1.664%

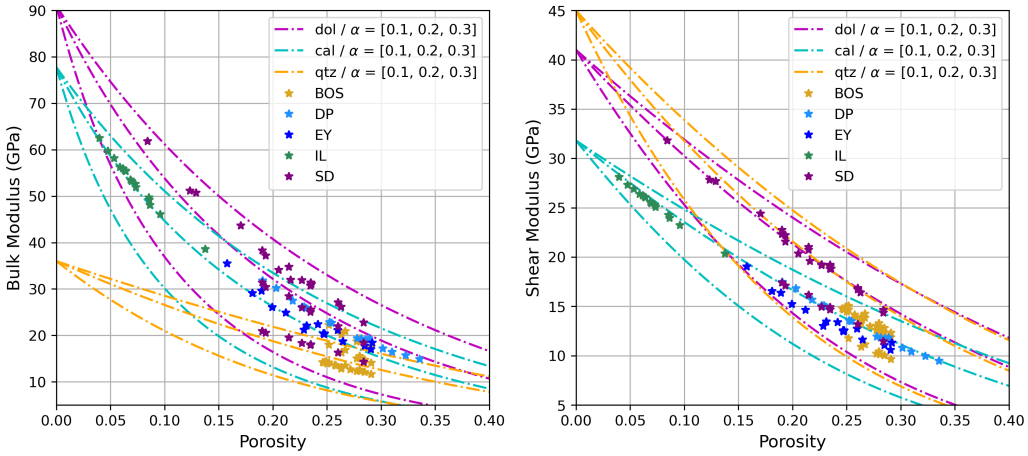


Figure 8. Bulk and shear moduli calculated using DRP numerical simulations in GeoDict. The stars represent the calculated porosity and elastic moduli of each sub-sample; the colors represent each sample type. The dashed-dotted lines represent the RPM predictions assuming different mineralogical compositions consistent with the samples for three different values of aspect ratios equal to 0.1, 0.2, and 0.3.

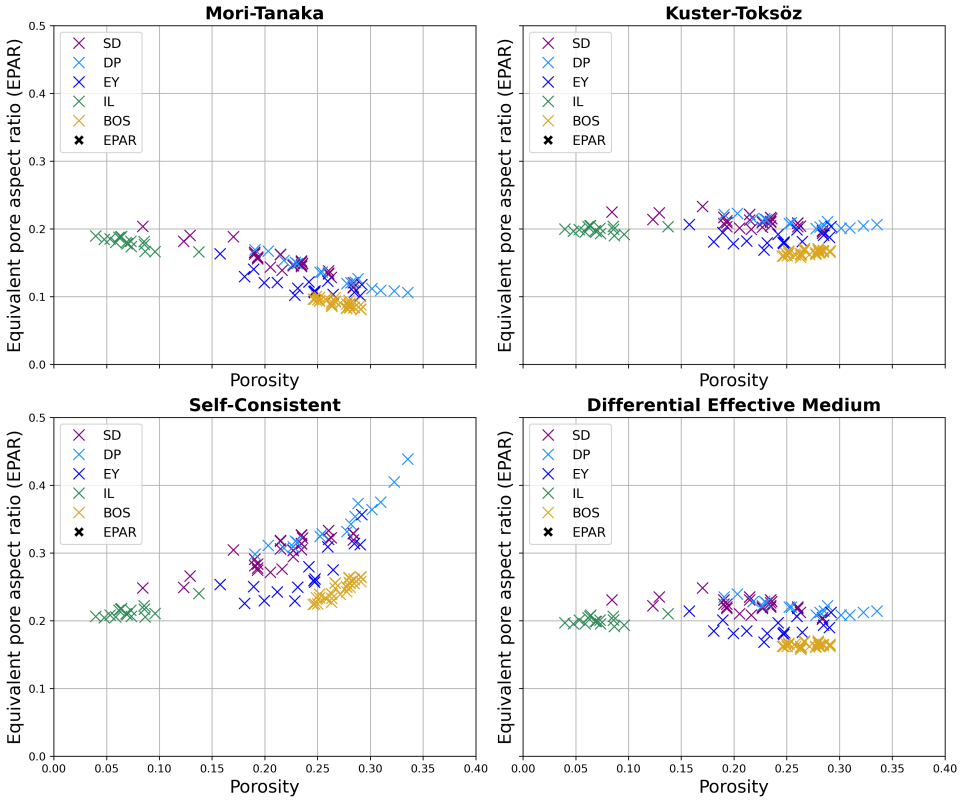


Figure 9. Estimated EPAR of digital images of 80 sub-samples for four RPMs. Each color represents a different rock type.

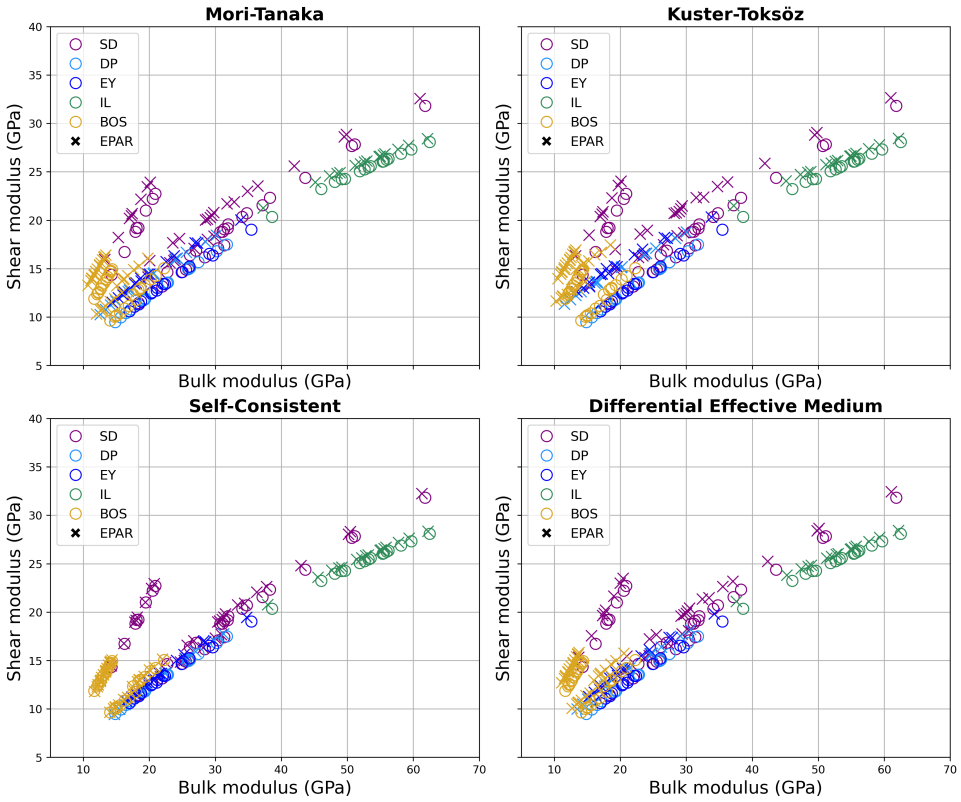


Figure 10. Estimated bulk and shear moduli of digital images of 80 sub-samples for four RPMs. Circles indicate values of elastic moduli numerically calculated using DRP; crosses indicate elastic moduli calculated using RPMs with the calculated EPARs. Each color represents a different rock type.

The mismatches between the RPM predictions and DRP simulations might be due to several sources of uncertainty, including the resolution of the DRP simulation, accuracy of the pore geometry description in the RPM, anisotropy, stress conditions, and natural variability and heterogeneity. Despite the high resolution of DRP models, the accuracy of the simulations depends on the ability to define the presentative elementary volume, especially in complex porous media, and compute continuous properties in the discretized digital domain. RPMs are generally accurate when the assumptions of the models are met; however, all models rely on idealized geometry describing the arrangement of the pore space and solid phase, and predictions might differ from the true values due to complex and heterogeneous structures.

3.3. Epar Calculation Based on RPM and Full Aspect Ratio Distribution

In this section, we demonstrate how to compute the EPAR using the rock physics model applied using the full distribution of aspect ratios. The aspect ratios are calculated using the GeoDict algorithm based on the watershed technique [34].

Using DRP tools, we estimate the distribution of aspect ratios in two real samples from a carbonate reservoir in a pre-salt region of the Santos basin, offshore Brazil. The two samples are from two different stratigraphic zones, Barra Velha and Itapema. In the following, we indicate with BVE the sample from lower Barra Velha and with ITP the sample from Itapema. The digital images are stored in grids of $600 \times 600 \times 600$ pixels with a resolution of 33.435 µm.

Figure 11 shows the distribution of the aspect ratio and the distribution of the aspect ratio weighted by the volume of the pores for both samples. Overall, the ITP sample shows lower aspect ratio values than the BVE sample. Figure 12 shows the separation of the pore space into individual objects, in 3D as well as on a 2D section, for both samples.

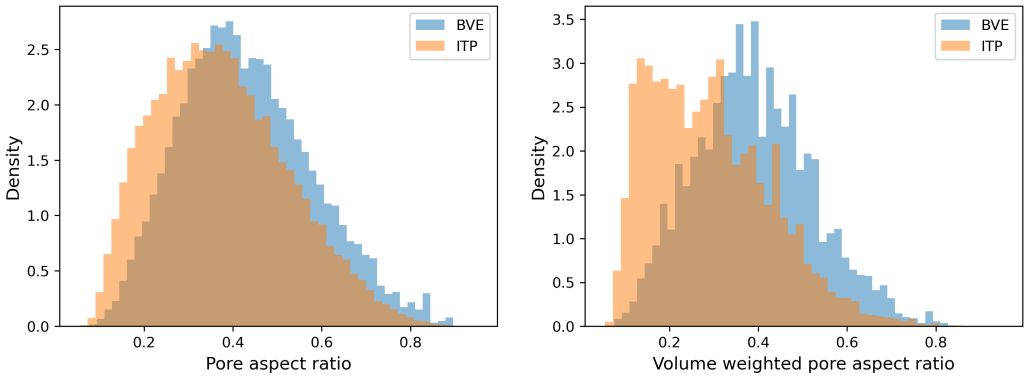


Figure 11. Aspect ratio distribution calculated from digital image analysis: on the (**left**), we show the distribution of aspect ratios; on the (**right**), we show the volume-weighted distribution of aspect ratios for sample BVE from lower Barra Velha formation (blue histograms) and sample ITP from Itapema formation (orange histograms).

We then estimate the EPAR according to two different approaches: (i) we estimate the EPAR by matching the DRM numerical simulations, and (ii) we estimate the EPAR by matching the RPM predictions obtained by applying the RPM with the full distribution of aspect ratios. We demonstrate the calculation of the EPAR using the SC model, but the same approach can be extended to the other models, although the extension to the DEM model is computationally expensive due to the large number of inclusions. To apply the rock physics model to the full distribution of aspect ratios, we discretize the values of aspect ratio in a set of 100 possible values. In other words, we assume that the porous rock is composed of 100 inclusions with corresponding values of aspect ratio α_p for $p = 1, \ldots, 100$. We then apply the RPM to compute the predictions of elastic moduli and then optimize the

EPAR values using Equation (10). We then compare the EPAR values to those obtained by optimizing Equation (10) using the DRP values of elastic moduli.

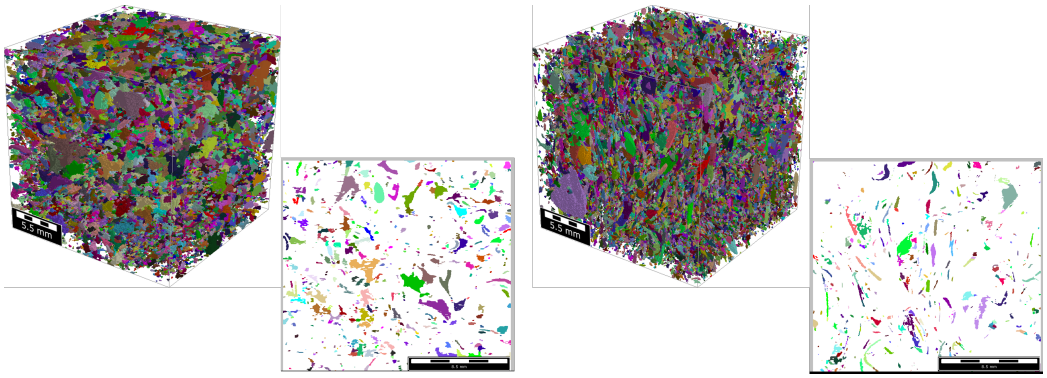


Figure 12. Pore space separation into individual objects (3D and 2D views) or sample BVE from lower Barra Velha formation (**left**) and sample ITP from Itapema formation (**right**). Each color represents an object considered as an individual pore.

Table 5 shows the results of the estimated EPAR values obtained from the DRP calculations and RPM model predictions for the two samples, BVE and ITP. For both samples, the two values are in good agreement. The EPAR values are also compared to the mean value of the distribution of aspect ratio; however, the obtained values are significantly lower, which proves that the EPAR is not a linear average of the aspect ratios but is more affected by lower values. Table 5 also shows the results of the estimated elastic moduli for the two samples, BVE and ITP, using the DRP numerical simulations, using RPM with a single inclusion with EPAR estimated from DRP simulations, using the RPM with the full distribution of aspect ratios, and using RPM with a single inclusion with EPAR estimated from RPM predictions. Overall, all these calculations are in good agreement.

Table 5. Estimated EPAR and elastic moduli numerically calculated using RPM predictions and DRP simulations for digital samples BVE and ITP from Brazilian pre-salt reservoir.

		BVE Sample	**ITP Sample**
EPAR	Mean of empirical distribution	0.3899	0.2923
	EPAR using RPM with full distribution	0.3187	0.2194
	EPAR using DRP numerical simulation	0.2882	0.2053
Bulk modulus (GPa)	DRP simulation	33.37	48.85
	RPM using DRP-based EPAR	32.98	48.49
	RPM using full distribution	34.65	49.66
	RPM using RPM-based EPAR	34.55	49.55
Shear modulus (GPa)	DRP simulation	18.27	24.26
	RPM using DRP-based EPAR	18.50	24.55
	RPM using full distribution	18.98	24.81
	RPM using RPM-based EPAR	18.94	24.78

3.4. Validation with Well Log Analysis

Synthetic samples were utilized to validate the application of numerical simulations for calculating effective elastic properties from 3D digital images. The numerical results align with the theoretical predictions from rock physics models across various porosities and inclusion types with differing aspect ratios. The results from real samples demonstrate that the inclusion models can accurately fit measurements of elastic properties.

To demonstrate the validity of the proposed investigation, we analyze the results using well log data from the carbonate reservoir from Brazil's pre-salt region in the Santos Basin, where the two core samples were extracted. The borehole goes through the basalt

outflows and siliciclastic deposits, coquinas and shales of the Camboriú, Piçarras, and Itapema formations, as well as the microbial lacustrine carbonates and evaporites in the Barra Velha and Ariri formations [44–48].

Figure 13 shows the petrophysical and elastic properties obtained from well log data and a simplified stratigraphic model. Dry bulk and shear moduli are calculated from sonic density logs using Gassmann's equation. The EPAR curve is computed by optimizing the RPM (the SC model in this application) to match the measured dry-rock bulk and shear moduli. Overall, the estimated EPAR shows higher values in the lower Barra Velha formation and lower values in the Itapema formation. The average values in the two formations are indicated with golden lines. These results are consistent with the DRP analysis.

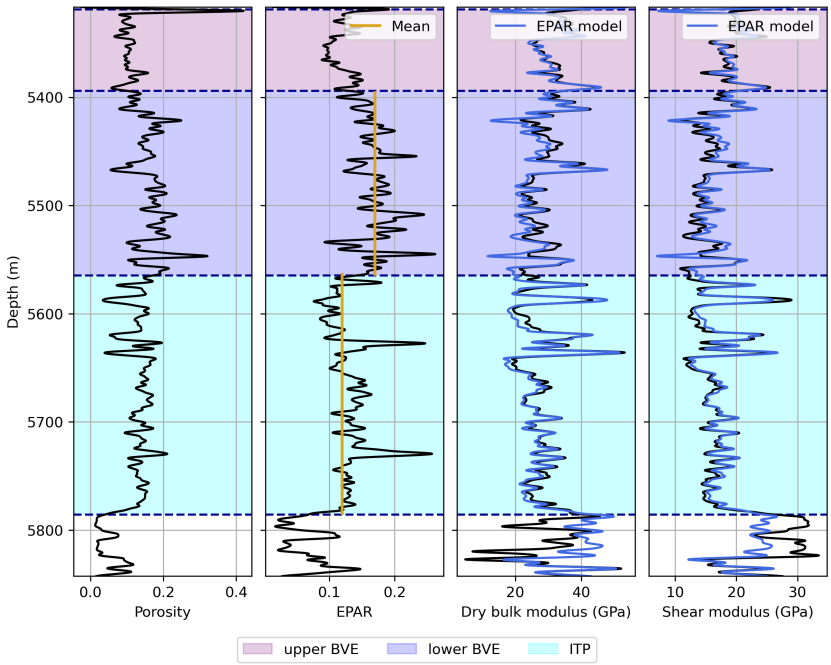


Figure 13. Measured and computed log data. From (**left**) to (**right**): porosity, estimated EPAR, and bulk and shear moduli. Black lines represent well logs, blue lines represent RPM predictions using EPAR, and golden lines represent EPAR mean values for each formation. The background colors represent stratigraphic zones corresponding to the intervals upper and lower Barra Velha and Itapema, respectively.

Figure 14 shows the measurements of bulk modulus from laboratory experiments and well log data. These results enable illustrating the difference in the pore geometry of rocks in different stratigraphic zones in the reservoir. Indeed, the thin sections of the two samples show more rounded pores in the lower Barra Velha sample and more elongated pores in the Itapema sample, consistent with the estimated EPAR values in the well log. This result is also consistent with the geological background. Indeed, coquinas in the Itapema formation typically consist of rudstones and grainstones of bivalve and gastropod shells [47], resulting in more elongated pore geometries, while the rocks of the Barra Velha formation are mostly composed of laminated carbonates, magnesian clay minerals, calcite spherulites, and shrubs [48,49], resulting in more rounded pores.

The proposed definition of EPAR is based on numerical optimization since the proposed model focuses on static reservoir characterization to estimate the pore geometry parameters, such as pore aspect ratio, at a specific time in the reservoir. The pore geometry parameters depend on diagenetic processes, such as compaction, dissolution, and cementation, and, as a consequence, they are correlated to reservoir properties such as pore volume,

permeability, flow rate, as well as the elastic and electrical properties such as elastic moduli, density, velocity, and electrical resistivity [1,16,41,44]

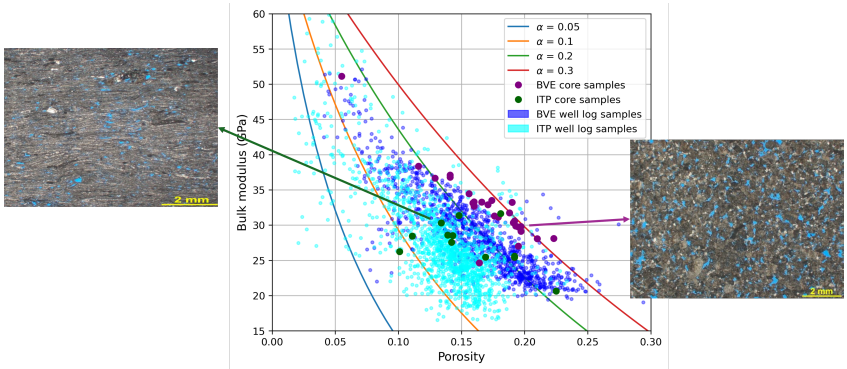


Figure 14. Crossplot of bulk modulus versus porosity for well log data. The smaller dots represent well log measurements, the larger dots represent the laboratory measurements in core samples, and the colored lines represent the rock physics model for different values of the aspect ratio. Two thin sections from core samples illustrate the different pore structure and shape in the stratigraphic zones. The colors represent three stratigraphic zones corresponding to the intervals upper and lower Barra Velha and Itapema.

4. Conclusions

This study presents a novel method to estimate an equivalent pore aspect ratio (EPAR) for improving rock physics model predictions in complex porous media. We first proved that the EPAR is not a linear average of the aspect ratios weighted by the volumetric proportions of the inclusions. Then, we demonstrated that the EPAR can be computed by minimizing the mismatch between measurements and predictions from rock physics models, providing a robust parameter for characterizing the spatial complexity of pore structures. Through validation using digital rock physics techniques, we demonstrated that the EPAR can be accurately derived from the full distribution of aspect ratios obtained from digital rock physics analysis. The results confirm the reliability of the EPAR approach and its ability to represent the effective elastic response of rocks with complex pore geometries. Furthermore, the findings justify the extension of the EPAR methodology to well log data for reservoir characterization. By enabling the characterization of pore structures in both synthetic and real core samples, the EPAR approach enhances the applicability of rock physics models in subsurface studies, particularly in carbonate reservoirs where pore complexity is significant. This work contributes to bridging the gap between theoretical models and practical applications, offering a framework for integrating rock physics models with digital rock physics and well log data to achieve more accurate subsurface characterizations. The proposed method can be extended to other geological environments characterized by the presence of fractures and micro-cracks. Hence, this approach can also be applied to map fractures in unconventional oil and gas reservoirs, as well as geothermal units.

Author Contributions: Conceptualization, L.E.Q. and D.G.; Methodology, L.E.Q.; Writing—original draft, L.E.Q. and D.G.; Writing—review and editing, C.P.F., T.M., L.P.d.F. and I.F.M. All authors have read and agreed to the published version of the manuscript.

Funding: This research received no external funding

Data Availability Statement: Data are available upon request.

Acknowledgments: The authors acknowledge Petrobras, the Federal University of Santa Catarina, and the University of Wyoming for support.

Conflicts of Interest: The authors declare no conflicts of interest.

Appendix A. Self-Consistent Approximation for Ellipsoidal Inclusions

For ellipsoidal inclusions ([7]), coefficients P_i^m and Q_i^m are provided by

$$P = \frac{1}{3}T_{iijj} \qquad \text{and} \qquad Q = \frac{1}{5}\left(T_{ijij} - \frac{1}{3}T_{iijj}\right) \tag{A1}$$

where

$$T_{iijj} = \frac{3F_1}{F_2} \qquad \text{and} \qquad T_{ijij} - \frac{1}{3}T_{iijj} = \frac{2}{F_3} + \frac{1}{F_4} + \frac{F_4F_5 + F_6F_7 - F_8F_9}{F_2F_4} \tag{A2}$$

with

$$\begin{aligned}
F_1 &= 1 + A\left[\frac{3}{2}(f+\theta) - R\left(\frac{3}{2}f + \frac{5}{2}\theta - \frac{4}{3}\right)\right] \\
F_2 &= 1 + A\left[1 + \frac{3}{2}(f+\theta) - (R/2)(3f+5\theta)\right] + B(3-4R) + \\
&\quad + (A/2)(A+3B)(3-4R)[f+\theta - R(f-\theta+2\theta^2)] \\
F_3 &= 1 + A\left[1 - \left(f + \frac{3}{2}\theta\right) + R(f+\theta)\right] \\
F_4 &= 1 + (A/4)[f + 3\theta - R(f-\theta)] \\
F_5 &= A\left[-f + R\left(f + \theta - \frac{4}{3}\right)\right] + B\theta(3-4R) \\
F_6 &= 1 + A[1 + f - R(f+\theta)] + B(1-\theta)(3-4R) \\
F_7 &= 2 + (A/4)[3f + 9\theta - R(3f+5\theta)] + B\theta(3-4R) \\
F_8 &= A[1 - 2R + (f/2)(R-1) + (\theta/2)(5R-3)] + B(1-\theta)(3-4R) \\
F_9 &- A[(R-1)f - R\theta] + B\theta(3-4R)
\end{aligned}$$

and A, B, and R provided by

$$A = \mu_i/\mu_m - 1 \tag{A3}$$

$$B = \frac{1}{3}(K_i/K_m - \mu_i/\mu_m) \tag{A4}$$

$$R = [(1-2\nu_m)/2(1-\nu_m)] \tag{A5}$$

and

$$\theta = \begin{cases} \dfrac{\alpha}{(\alpha^2-1)^{3/2}}\left[\alpha(\alpha^2-1)^{1/2} - \cosh^{-1}\alpha\right] \\ \dfrac{\alpha}{(1-\alpha^2)^{3/2}}\left[\cos^{-1}\alpha - \alpha(\alpha^2-1)^{1/2}\right] \end{cases} \tag{A6}$$

for prolate ($\alpha > 1$) and oblate ($\alpha < 1$) spheroids, respectively, and

$$f = \frac{\alpha^2}{1-\alpha^2}(3\theta - 2) \tag{A7}$$

where α is the pore aspect ratio.

References

1. Mavko, G.; Mukerji, T.; Dvorkin, J. *The Rock Physics Handbook: Tools for Seismic Analysis of Porous Media*, 2 ed.; Cambridge University Press: Cambridge, UK, 2009. [CrossRef]
2. Eberli, G.P.; Baechle, G.T.; Anselmetti, F.S.; Incze, M.L. Factors controlling elastic properties in carbonate sediments and rocks. *Geophysics* **2003**, *22*, 654–660. [CrossRef]
3. Vasquez, G.F.; Morschbacher, M.J.; dos Anjos, C.W.D.; Silva, Y.M.P.; Madrucci, V.; Justen, J.C.R. Petroacoustics and composition of presalt rocks from Santos Basin. *Lead. Edge* **2019**, *38*, 342–348. [CrossRef]
4. Budiansky, B. On the elastic moduli of some heterogeneous materials. *J. Mech. Phys. Solids* **1965**, *13*, 223–227. [CrossRef]

5. Mori, T.A.; Tanaka, K. Average stress in matrix and average elastic energy of materials with misfitting inclusions. *Acta Metall.* **1973**, *21*, 571–574. [CrossRef]
6. Kuster, G.T.; Toksöz, M.N. Velocity and Attenuation of SeismicC Waves in Two-phase Media: Part I. Theoretical Formulations. *Geophysics* **1974**, *39*, 587–606. [CrossRef]
7. Berryman, J.G. Long-wavelength propagation in composite elastic media I. Spherical inclusions. *J. Acoust. Soc. Am.* **1980**, *68*, 1809–1819. [CrossRef]
8. Berryman, J.G. Elastic wave propagation in fluid-saturated porous media. *J. Acoust. Soc. Am.* **1981**, *69*, 416–424. [CrossRef]
9. Norris, A. A differential scheme for the effective moduli of composites. *Mech. Mater.* **1985**, *4*, 1–16. [CrossRef]
10. Garboczi, E.J.; Berryman, J.G. Elastic moduli of a material containing composite inclusions: effective medium theory and finite element computations. *Mech. Mater.* **2001**, *33*, 455–470. [CrossRef]
11. Xu, S.; Payne, M.A. Modeling elastic properties in carbonate rocks. *Lead. Edge* **2009**, *28*, 66–74. [CrossRef]
12. Sun, Y.F. Pore structure effects on elastic wave propagation in rocks: AVO modelling. *J. Geophys. Eng.* **2004**, *1*, 268–276. [CrossRef]
13. Dou, Q.; Sun, Y.; Sullivan, C. Rock-physics-based carbonate pore type characterization and reservoir permeability heterogeneity evaluation, Upper San Andres reservoir, Permian Basin, west Texas. *J. Appl. Geophys.* **2011**, *74*, 8–18. [CrossRef]
14. Li, T.; Wang, Z.; Gu, Y.J.; Wang, R.; Wang, Y. Experimental study of fracture structure effects on acoustic logging data using a synthetic borehole model. *J. Pet. Sci. Eng.* **2019**, *183*, 106433. [CrossRef]
15. Grechka, V.; Kachanov, M. Effective elasticity of rocks with closely spaced and intersecting cracks. *Geophysics* **2006**, *71*, D85–D91. [CrossRef]
16. Fournier, F.; Léonide, P.; Kleipool, L.; Toullec, R.; Reijmer, J.J.; Borgomano, J.; Klootwijk, T.; Van Der Molen, J. Pore space evolution and elastic properties of platform carbonates (Urgonian limestone, Barremian—Aptian, SE France). *Sediment. Geol.* **2014**, *308*, 1–17. [CrossRef]
17. Wang, Z.; Wang, R.; Wang, F.; Qiu, H.; Li, T. Experiment study of pore structure effects on velocities in synthetic carbonate rocks. *Geophysics* **2015**, *80*, D207–D219. [CrossRef]
18. Dias, J.; Lopez, J.L.; Velloso, R.; Perosi, F. A workflow for multimineralogic carbonate rock physics modelling in a Bayesian framework: Brazilian pre-salt reservoir case study. *Geophys. Prospect.* **2021**, *69*, 650–676. [CrossRef]
19. Pillar, N.; Yan, J.; Lubbe, R. Variable Aspect Ratio Method in the Xu-White Model for AVO. In Proceedings of the 69th EAGE Conference and Exhibition incorporating SPE EUROPEC 2007, London, UK, 11–14 June 2007; European Association of Geoscientists & Engineers: Utrecht, The Netherlands, 2007. [CrossRef]
20. Cilli, P.; Chapman, M. Modelling the Elastic and Electrical Properties of Rocks with Complex Pore Geometries. In Proceedings of the 80th EAGE Conference and Exhibition 2018, Copenhagen, Denmark, 11–14 June 2018; European Association of Geoscientists & Engineers: Utrecht, The Netherlands, 2018; Volume 2018, pp. 1–5. [CrossRef]
21. Dvorkin, J.; Derzhi, N.; Diaz, E.; Fang, Q. Relevance of computational rock physics. *Geophysics* **2011**, *76*, E141–E153. [CrossRef]
22. Andrä, H.; Combaret, N.; Dvorkin, J.; Glatt, E.; Han, J.; Kabel, M.; Keehm, Y.; Krzikalla, F.; Lee, M.; Madonna, C.; et al. Digital rock physics benchmarks—Part I: Imaging and segmentation. *Comput. Geosci.* **2013**, *50*, 25–32. [CrossRef]
23. Saenger, E.H.; Vialle, S.; Lebedev, M.; Uribe, D.; Osorno, M.; Duda, M.; Steeb, H. Digital carbonate rock physics. *Solid Earth* **2016**, *7*, 1185–1197. [CrossRef]
24. Weger, R.J.; Eberli, G.P.; Baechle, G.T.; Massaferro, J.L.; Sun, Y.F. Quantification of pore structure and its effect on sonic velocity and permeability in carbonates. *AAPG Bull.* **2009**, *93*, 1297–1317. [CrossRef]
25. Weger, R.J.; Eberli, G.P.; Massaferro, J.L.; Sun, Y.; Baechle, G.T. Theoretically derived pore geometry in carbonates using the extended biot theory. *Mar. Pet. Geol.* **2023**, *155*, 106359. [CrossRef]
26. Andrä, H.; Combaret, N.; Dvorkin, J.; Glatt, E.; Han, J.; Kabel, M.; Keehm, Y.; Krzikalla, F.; Lee, M.; Madonna, C.; et al. Digital rock physics benchmarks—Part II: Computing effective properties. *Comput. Geosci.* **2013**, *50*, 33–43. [CrossRef]
27. Zhao, L.; Nasser, M.; Han, D.H. Quantitative geophysical pore-type characterization and its geological implication in carbonate reservoirs. *Geophys. Prospect.* **2013**, *61*, 827–841. [CrossRef]
28. Teillet, T.; Fournier, F.; Zhao, L.; Borgomano, J.; Hong, F. Geophysical pore type inversion in carbonate reservoir: Integration of cores, well logs, and seismic data (Yadana field, offshore Myanmar). *Geophysics* **2021**, *86*, B149–B164. [CrossRef]
29. Guo, Q.; Ba, J.; Luo, C. Nonlinear petrophysical amplitude variation with offset inversion with spatially variable pore aspect ratio. *Geophysics* **2022**, *87*, M111–M125. [CrossRef]
30. Guo, Q.G.; Ba, J.; Luo, C. Seismic rock-physics linearized inversion for reservoir-property and pore-type parameters with application to carbonate reservoirs. *Geoenergy Sci. Eng.* **2023**, *224*, 211640. [CrossRef]
31. Wang, G.; Chen, S.; Wang, Y. Direct inversion for the equivalent pore aspect ratio based on the theory of ellipsoid modelling. *Geophys. Prospect.* **2022**,*71*, 1821–1834. [CrossRef]
32. Berryman, J.G. Mixture theories for rock properties. *Rock Phys. Phase Relat. Handb. Phys. Constants* **1995**, *3*, 205–228.
33. Garboczi, E. *Finite Element and Finite Difference Programs for Computing the Linear Electric and Elastic Properties of Digital Images of Random Materials*; National Institute of Standards and Technology: Gaithersburg, MD, USA, 1998. [CrossRef]

34. *GeoDict Simulation Software Relase*; Math2Market GmbH: Kaiserslautern, Germany, 2024. [CrossRef]
35. Kabel, M.; Merkert, D.; Schneider, M. Use of composite voxels in FFT-based homogenization. *Comput. Methods Appl. Mech. Eng.* **2015**, *294*, 168–188. [CrossRef]
36. Avizo Software. Available online: http://www.thermofisher.com/avizo (accessed on 10 February 2025).
37. Buades, A.; Coll, B.; Morel, J.M. A non-local algorithm for image denoising. In Proceedings of the 2005 IEEE Computer Society Conference on Computer Vision and Pattern Recognition (CVPR'05), San Diego, CA, USA, 20–25 June 2005; Volume 2, pp. 60–65.
38. Sheppard, A.P.; Sok, R.M.; Averdunk, H. Techniques for image enhancement and segmentation of tomographic images of porous materials. *Phys. A Stat. Mech. Its Appl.* **2004**, *339*, 145–151. [CrossRef]
39. Vincent, L.; Soille, P. Watersheds in digital spaces: An efficient algorithm based on immersion simulations. *IEEE Trans. Pattern Anal. Mach. Intell.* **1991**, *13*, 583–598. [CrossRef]
40. Gonzalez, R.; Woods, R. *Digital Image Processing*; Pearson: London, UK, 2018.
41. Fournier, F.; Leonide, P.; Biscarrat, K.; Gallois, A.; Borgomano, J.; Foubert, A. Elastic properties of microporous cemented grainstones. *Geophysics* **2011**, *76*, E211–E226. [CrossRef]
42. GeoSlicer. Available online: https://www.ltrace.com.br/geoslicer/ (accessed on 10 February 2025).
43. Carneiro, I.B.; Souza, J.V.B.d.; Zanelatto, D.E.; Mei, M.K.R.; Sapucaia, V.W.; Figueiredo, L.P.d.; Bordignon, F.L.; Matias, J.L.d.L.; Honório, B.C.Z.; Surmas, R. Multiscale analysis of carbonate rocks for the digital rocks platform GeoSlicer, an open source plugin. In Proceedings of the Rio Oil & Gas, Rio de Janeiro, RJ, Brazil, 23–26 September 2024.
44. Fournier, F.; Pellerin, M.; Villeneuve, Q.; Teillet, T.; Hong, F.; Poli, E.; Borgomano, J.; Léonide, P.; Hairabian, A. The equivalent pore aspect ratio as a tool for pore type prediction in carbonate reservoirs. *AAPG Bull.* **2018**, *102*, 1343–1377. [CrossRef]
45. Lima, B.E.M.; De Ros, L.F. Deposition, diagenetic and hydrothermal processes in the Aptian Pre-Salt lacustrine carbonate reservoirs of the northern Campos Basin, offshore Brazil. *Sediment. Geol.* **2019**, *383*, 55–81. [CrossRef]
46. Silva Adriano, M.; Figueiredo, J.P.; Coelho, P.H.G.R.; Borghi, L. Tectonic and stratigraphic evolution of the Santos Basin rift phase: New insights from seismic interpretation on Tupi oil field area. *J. S. Am. Earth Sci.* **2022**, *116*, 103842. [CrossRef]
47. Chinelatto, G.F.; Belila, A.M.P.; Basso, M.; Souza, J.P.P.; Vidal, A.C. A taphofacies interpretation of shell concentrations and their relationship with petrophysics: A case study of Barremian-Aptian coquinas in the Itapema Formation, Santos Basin-Brazil. *Mar. Pet. Geol.* **2020**, *116*, 104317. [CrossRef]
48. Rebelo, T.B.; Batezelli, A.; Mattos, N.H.; Leite, E.P. Sedimentary processes and paleoenvironment reconstruction of the Barra Velha formation, Santos Basin, Brazilian pre-salt. *Mar. Pet. Geol.* **2023**, *150*, 106141. [CrossRef]
49. Gomes, J.; Bunevich, R.; Tedeschi, L.; Tucker, M.; Whitaker, F. Facies classification and patterns of lacustrine carbonate deposition of the Barra Velha Formation, Santos Basin, Brazilian Pre-salt. *Mar. Pet. Geol.* **2020**, *113*, 104176. [CrossRef]

Disclaimer/Publisher's Note: The statements, opinions and data contained in all publications are solely those of the individual author(s) and contributor(s) and not of MDPI and/or the editor(s). MDPI and/or the editor(s) disclaim responsibility for any injury to people or property resulting from any ideas, methods, instructions or products referred to in the content.